UNVEILING THE COSMIC DAWN AND EPOCH OF REIONIZATION USING COSMIC 21-CM SIGNAL

Synopsis (approx. 5000 words)

Submitted for the partial fulfillment of the requirements for the degree of Doctor of Philosophy in Science

by

Ankita Bera

Under the supervision of

Dr. Saumyadip Samui

&

Dr. Kanan Kumar Datta

School of Astrophysics
Presidency University
Kolkata, India
2023

UNVEILING THE COSMIC DAWN AND EPOCH OF REIONIZATION USING COSMIC 21-CM SIGNAL

Name of the Candidate : Ankita Bera

Registration Number : R-18RS09160150

Date of Registration : 28 August, 2019

Department : School of Astrophysics

Institution : Presidency University

Signature :

Date :

List of Publications:

- **Published manuscripts:**

  1. Primordial magnetic fields during the cosmic dawn in light of EDGES 21-cm signal; **Ankita Bera**, Kanan Kumar Datta, Saumyadip Samui, **MNRAS** 498, 1, (2020).
  2. Cosmic recombination history in light of EDGES measurements of the cosmic dawn 21-cm signal; Kanan K. Datta, Aritra Kundu, Ankit Paul, **Ankita Bera**, **Physical Review D**, 102, 8, 083502, (2020).
  3. Studying Cosmic Dawn using redshifted HI 21-cm signal: A brief review; **Ankita Bera**, Raghunath Ghara, Atrideb Chatterjee, Kanan K. Datta, Saumyadip Samui, **Journal of Astrophysics and Astronomy**, 44, 1, (2023).
  4. Impact of cosmic rays on the global 21-cm signal during cosmic dawn; **Ankita Bera**, Saumyadip Samui, and Kanan K. Datta, **MNRAS**, 519, 4, (2023).

- **Communicated manuscripts:**

  1. Bridging the gap between Cosmic Dawn and Reionization favors Faint Galaxies-dominated Models; **Ankita Bera**, Sultan Hassan, Aaron Smith, Renyue Cen, Enrico Garaldi, Rahul Kannan, and Mark Vogelsberger ; Under review in **ApJ**, (2022), [https://ui.adsabs.harvard.edu/abs/2022arXiv220914312B].

Contributed talks in National and International conferences:

- **International conferences:**

  1. 5th Global 21-cm Workshop at University of California, Berkeley, USA, October 17-20, 2022, **Talk**: *Bridging the Gap between Cosmic Dawn and Reionization favors Faint Galaxies-dominated Models.*
  2. Reionization on a blackboard Conference at CCA, Flatiron Institute, USA, September 19-22, 2022, **Flash Talk**: *Bridging the Gap between Cosmic Dawn and Reionization.*
  3. 8th Annual Science At Low Frequencies (SALF) Conference, hosted virtually by the University of Amsterdam, December 6-9, 2021, **Talk**: *Impact of cosmic ray heating on global 21-cm signal during cosmic dawn.*
  4. Virtual SKA Science Conference: A precursor view of the SKA Sky, hosted virtually by the SKA Observatory, March 15-19, 2021, **Talk**: *Non-standard heating of the IGM during the cosmic dawn.*
  5. International Conference and School on Observing The First Billion Years of the Universe Using Next Generation Telescopes at IIT Indore, India, January 20-31, 2020, **Talk**: *Effects of primordial magnetic field on the 21cm signal from cosmic dawn.*

- **National conferences:**

  1. Workshop on 21-cm Cosmology in the Square Kilometre Array Era at Indian Statistical Institute, Kolkata, India, October 31 - November 4, 2022, **Talk**: *Impact of cosmic ray heating on global 21-cm signal during cosmic dawn.*
  2. The 39th Annual Meeting of the Astronomical Society of India (ASI), virtually hosted by ICTS-TIFR Bengaluru, IISER Mohali, IIT Indore and IUCAA Pune, February 18-23, 2021, **Talk**: *Primordial magnetic fields during the cosmic dawn in light of EDGES 21-cm signal.*

1 Cosmic Dawn and Epoch of Reionization: an overview

The universe came into existence with a Big Bang approximately 13.6 billion years ago. Universe got cooled as it expanded adiabatically, and over time, different ingredients of our Universe such as quarks, protons, neutrons, and then electrons froze out. Finally, about 370,000 years after the Big Bang, hydrogen started to form by recombination of protons with the free electrons. With the formation of these first hydrogen atoms, the universe entered a period called the 'Dark Ages'. During this time, hydrogen was mostly neutral until the first stars, quasars, and/or the first generation of galaxies appeared. The ignition of the first stars marked the end of the Dark Ages and the beginning of 'Cosmic Dawn' (CD). It happened approximately 100 million years after the Big Bang. However, it is extremely difficult to directly observe these early Universe faint sources as they are beyond the reach of our present-day telescopes. Therefore, observations of redshifted 21-cm signal from the neutral hydrogen (HI) have become the most promising tool for studying the cosmic dawn (Furlanetto et al., 2006a; Pritchard & Loeb, 2012; Cooray et al., 2019; Padmanabhan, 2021) and the subsequent 'Epoch of Reionization' (EoR).

There are mainly two separate approaches by which the cosmological HI 21-cm signal from the CD/EoR can be detected, namely, the measurements of (i) global HI 21-cm signal, and, (ii) statistical signal such as power spectrum, Bi-spectrum etc. Several ongoing and upcoming experiments such as the Experiment to Detect the Global reionization Signature (EDGES, Bowman et al., 2018), Shaped Antenna measurement of the background RAdio Spectrum (SARAS, Singh et al., 2021), Large-Aperture Experiment to Detect the Dark Ages (LEDA, Price et al., 2018), the Radio Experiment for the Analysis of Cosmic Hydrogen (REACH, De & Acedo, 2019) etc. are dedicated to detect the global HI 21-cm signal. The recent observations of global HI 21-cm absorption signal by experiments such as the Experiment to Detect the Epoch of Reionization Signature (EDGES) (Bowman et al., 2018) have opened up the possibilities to study the evolution of the early stars and galaxies and the thermal state of the inter-galactic medium (IGM) during cosmic dawn. The detected signal has an absorption depth of $0.5^{+0.5}_{-0.2}$ K centred at frequency 78 ± 1 MHz or redshift $z \sim 17$. The 'U' shaped 21-cm signal caries signatures of early Lyman-α (Ly-α) coupling and heating of the IGM in the redshift range of $\sim 14-22$. However, there seems to be quite controversity exists with the detected EDGES signal. For example, recent observations by Shaped Antenna measurement of the background RAdio Spectrum (SARAS 3) (Singh et al., 2021) has claimed that the EDGES profile may not be of astrophysical origin. There are also concerns that the unusualities in the signal may arise

due to unaccounted systematics (Hills et al., 2018; Bradley et al., 2019; Singh & Subrahmanyan, 2019; Sims & Pober, 2020). Nonetheless, several explanations have been proposed in order to explain the unusual absorption trough as the absorption depth of the detected signal is almost two times larger than the strongest prediction (see e.g., Barkana, 2018; Muñoz & Loeb, 2018; Mebane et al., 2020; Ewall-Wice et al., 2020).

However, the global HI 21-cm signal can not retain information regarding the spatial distribution of HI field and sources, and provide only the global evolution of the HI differential brightness temperature. Radio interferometric telescopes such as the Giant Metrewave Radio Telescope (GMRT, Ali et al., 2008; Pal et al., 2021), the Murchison Widefield Array (MWA, Beardsley et al., 2016; Patwa et al., 2021), Low Frequency Array (LOFAR, Patil et al., 2017; Mertens et al., 2020), the Hydrogen Epoch of Reionization Array (HERA, DeBoer et al., 2017; Abdurashidova et al., 2022), and the Square Kilometre Array (SKA, Mellema et al., 2015) are devoted to probe the spatial fluctuations in the HI 21-cm signal during cosmic dawn and reionization. Moreover, the SKA should also be able to provide images of HI 21-cm field along with the statistical signal coming from cosmic dawn and EoR.

Inspired by these upcoming and future observations, we devoted our work in understanding the physical mechanisms that impact the global HI 21-cm signal. Furthermore, we combine constraints derived from the observation of global 21-cm signal along with the observations from reionization and post-reionization epoch to shed light on the faint end of the UV luminosity function. The relevant physics describing the 21-cm signal is elaborated in the sec. 2. Our study on two types of heating sources namely, primordial magnetic field (PMF) and cosmic rays are described in sec. 3 and 4 respectively. We present the detailed mechanisms of these heating processes and their impact on gas kinetic temperature (T_g), spin temperature (T_s), and the corresponding brightness temperature (T_{21}) during cosmic dawn and EoR. We also model Ly-α radiation background during cosmic dawn and incorporate the Ly-α coupling effect while modeling the global HI 21-cm signal. Moreover, our model considers both Population III (hereafter, Pop III) and Population II (hereafter, Pop II) sources. In sec. 5, we explore a source model derived from radiative transfer hydrodynamic simulation. We then calibrate our model with recent measurements of global HI 21-cm signal from CD and with several reionization observables to explore the joint parameter space to determine the range of models that naturally reproduce the combined constraints from reionization and cosmic dawn. Finally, in sec. 6, we discuss and summarise our main results obtained. Throughout this article we assume a flat,

ΛCDM cosmology with the cosmological parameters obtained from recent Planck 2018 (Planck Collaboration et al., 2020a) observation, i.e. $\Omega_\Lambda = 0.69$, $\Omega_{\rm m} = 0.31$, $\Omega_{\rm b} = 0.049$, and the Hubble parameter $H_0 = 67.66$ km/s/Mpc, unless otherwise mentioned.

2 Global HI 21-cm signal

The redshifted 21-cm radio signal is received from the early universe due to the presence of neutral hydrogen (see, eg. Pritchard & Loeb, 2012; Furlanetto et al., 2006b; Bera et al., 2023a, for brief reviews on cosmic 21-cm signal). The globally averaged HI differential brightness temperature (T_{21}) is a measure of the redshifted 21-cm signal at redshift z, and can be written as (Pritchard & Loeb, 2012),

$$T_{21} \approx 27 \times 10^{-3} x_{\rm HI} \left(1 - \frac{T_\gamma}{T_s}\right) \left(\frac{\Omega_{\rm b} h^2}{0.02}\right) \left(\frac{0.15}{\Omega_{\rm m} h^2}\right)^{0.5} \left(\frac{1+z}{10}\right)^{0.5} {\rm K}. \tag{1}$$

Here, T_γ is the temperature of the background radio emission which is dominated by the CMBR and T_s is the hydrogen spin temperature which is determined by the relative population of the two hydrogen ground state hyperfine levels. Further, $x_{\rm HI}$ is the mass averaged neutral hydrogen fraction which is determined by the physical processes such as recombination, photoionization and collisional ionization. The mass averaged ionization fraction x_e ($= 1 - x_{\rm HI}$) prior to formation of first luminous objects can be calculated as (Peebles, 1968),

$$\frac{dx_e}{dz} = \frac{1}{H(z)\,(1+z)} \left[C_p \left(\alpha_e\, x_e^2 n_{\rm H} - \beta_e\,(1-x_e)\, e^{-\frac{h_p \nu_\alpha}{k_B T_g}} \right) - \gamma_e\, n_H (1-x_e) x_e \right]. \tag{2}$$

Here, C_p is the Peeble's factor, h_p is the Planck's constant, α_e is the recombination co-efficient, β_e is the photoionization coefficient as given in Seager et al. (1999, 2000) and γ_e is the collisional ionization coefficient (Minoda et al., 2017).

T_s in Eq. 1 is governed by three coupling mechanisms: (i) radiative transition due to the absorption and stimulated emission of CMB photons (couples T_s and T_γ), (ii) spin flip transition due to atomic collisions (couples T_s and T_g) and (iii) the Wouthuysen-Field effect (Wouthuysen, 1952; Field, 1959), which can be obtained using,

$$1 - \frac{T_\gamma}{T_s} = \frac{x_{\rm tot}}{1 + x_{\rm tot}} \left(1 - \frac{T_\gamma}{T_g}\right), \tag{3}$$

where, $x_{\rm tot} = x_\alpha + x_c$, the sum of the coupling coefficients due to scattering of Ly-α photons and atomic collisions respectively (Wouthuysen, 1952; Field, 1958). As soon as the first generation

of stars forms, they emit photons at a range of frequencies, including at frequencies higher than Ly-α photons. Photons with frequency between Ly-α and Ly-β get redshifted directly into the Ly-α resonance. The photons having frequency between Ly-γ and Ly-limit get redshifted into nearest Lyman series resonance and then excite ground state hydrogen atoms. These excited HI atoms decay back to $1s$ through radiative cascading process and eventually terminate either in Ly-α photons or in two $2s \rightarrow 1s$ photons. Subsequently, the singlet and triplet HI hyperfine level population is altered through Ly-α absorption and emission which is known as the Wouthuysen-Field effect. As the HI spin temperature is determined by the relative population of these hyperfine states, T_s gets affected due to the presence of Ly-α photons. This Ly-α mechanism determines the coupling and decoupling of spin temperature T_s to the gas temperature T_g which, in turn, determines the onset of 21-cm absorption signal. Thus, we incorporate the Ly-α flux while calculating the 21-cm signal, and we mostly follow Barkana & Loeb (2005); Hirata (2006) and Pritchard & Furlanetto (2006) in our work to do so (see Bera et al., 2023b, for all the relevant equations that we used to calculate the flux of Ly-α).

The evolution of the IGM kinetic temperature, T_g as a function of redshift can be obtained by solving the equation (Kompaneets, 1957; Peebles, 1993; Seager et al., 1999),

$$\frac{dT_g}{dz} = \frac{2T_g}{1+z} - \frac{8\sigma_T a_{\rm SB} T_\gamma^4}{3m_e c H(z)(1+z)} \left(T_\gamma - T_g\right) \frac{x_e}{1+x_e} - \frac{2}{3k_B} \sum_i Q_i. \tag{4}$$

Here, $k_{\rm B}$, $\sigma_{\rm T}$ are the Boltzmann constant, Thomson scattering cross-section respectively and $a_{\rm SB} = 4\sigma_{\rm SB}/c$, where $\sigma_{\rm SB}$ is the Stefan Boltzmann constant. The third term Q_i includes the heating and cooling mechanisms such as heating due to primordial magnetic field (PMF), X-ray photons, cosmic rays (CRs) and cooling/heating due to the possible interaction between dark matter and baryons etc. The energy transfer rate from dark matters to baryons due to such interactions can be modelled as (Muñoz et al., 2015),

$$\frac{dQ_b}{dt} = \frac{2m_b \rho_\chi \sigma_0 e^{-r^2/2} (T_\chi - T_g) k_B c^4}{(m_b + m_\chi)^2 \sqrt{2\pi} u_{\rm th}^3} + \frac{\rho_\chi}{\rho_m} \frac{m_\chi m_b}{m_\chi + m_b} V_{\chi b} \frac{D(V_{\chi b})}{c^2}, \tag{5}$$

where, m_χ, m_b and ρ_χ, ρ_b are the masses and energy densities of dark matter and baryon respectively. The dark matter temperature is represented as, T_χ. The variance of the thermal relative velocity of dark matter and baryon fluids is given by $u_{\rm th}^2 = k_B(T_b/m_b + T_\chi/m_\chi)$, $V_{\chi b}$ is the relative velocity, and $D(V_{\chi b})$ is the drag term (see Datta et al., 2020, for all the equations that we used to model the dark matter-baryon interaction).

The rise in the global HI 21-cm absorption signal in the redshift range $z \sim 16-14$ requires the IGM temperature to increase very rapidly to match with the background radio temperature.

The X-ray heating by the first generation of galaxies/black holes is one such possibility which has been widely studied (Pritchard & Furlanetto, 2007; Fialkov et al., 2014; Das et al., 2017; Ma et al., 2021). Among the other possibilities, such as heating due to the primordial magnetic field (Sethi & Subramanian, 2005; Bera et al., 2020), shocks (Xu et al., 2021), cosmic rays (Ginzburg & Ozernoi, 1966; Samui et al., 2005; Sazonov & Sunyaev, 2015; Bera et al., 2023b), Ly-α photons (Madau et al., 1997; Chuzhoy & Shapiro, 2006; Ghara & Mellema, 2020; Mittal & Kulkarni, 2021), CMB photons (Venumadhav et al., 2018), heating due to PMF and CRs have been described in the following sections.

3 IGM heating due to primordial magnetic field during cosmic dawn*

Magnetic field exerts Lorentz force on the ionized component of the IGM. This causes rise in the IGM temperature, T_g. There are mainly two processes namely the ambipolar diffusion (AD) and decaying turbulence (DT) by which the magnetic field can heat up the IGM during the cosmic dawn and dark ages. We follow the prescription presented in Sethi & Subramanian (2005) and Chluba et al. (2015) to calculate the rate of heating due to these two processes. The heating rate (in unit of energy per unit time per unit volume) due to the ambipolar diffusion is given by,

$$\Gamma_{\rm AD} = \frac{(1-x_e)}{\gamma x_e \rho_b^2} \frac{\left\langle |(\nabla \times \boldsymbol{B}) \times \boldsymbol{B}|^2 \right\rangle}{16\pi^2}, \tag{6}$$

where $x_e = n_e/n_{\rm H}$ is the residual free electron fraction and $n_{\rm H} = n_{\rm HI} + n_{\rm HII}$. We assume $n_{\rm HII} = n_e$ as Helium is considered to be fully neutral in the redshift range of our interest. Further, ρ_b is the baryon mass density at redshift z, and the coupling coefficient between the ionized and neutral components is $\gamma = \langle \sigma v \rangle_{HH^+}/2m_H = 1.94 \times 10^{14}\,(T_g/{\rm K})^{0.375}\,{\rm cm^3 gm^{-1} s^{-1}}$. The Lorentz force can be approximated as $\left\langle |(\nabla \times \boldsymbol{B}) \times \boldsymbol{B}|^2 \right\rangle \approx 16\pi^2 \rho_B(z)^2 l_d(z)^{-2} f_L(n_B+3)$ (Chluba et al., 2015), where $\rho_B(z) = |\mathbf{B}|^2/8\pi$ is the magnetic field energy density at redshift z, $f_L(p) = 0.8313[1 - 1.02 \times 10^{-2} p]p^{1.105}$, and $l_d^{-1} = (1+z)\,k_D$. The damping scale is given by $k_D \approx 286.91\,(B_0/{\rm nG})^{-1}\,{\rm Mpc}^{-1}$ (Kunze & Komatsu, 2014).

*This section is adapted from the paper, "Primordial magnetic fields during the cosmic dawn in light of EDGES 21-cm signal" by Bera et al. (2020).

The heating rate due to the decaying turbulence is described by,

$$\Gamma_{\rm DT} = \frac{3m}{2} \frac{\left[\ln\left(1+\frac{t_i}{t_d}\right)\right]^m}{\left[\ln\left(1+\frac{t_i}{t_d}\right)+\frac{3}{2}\ln\left(\frac{1+z_i}{1+z}\right)\right]^{m+1}} H(z)\,\rho_B(z), \tag{7}$$

where $m = 2\,(n_B+3)/(n_B+5)$, and n_B is the spectral index corresponding to the primordial magnetic field. The physical decay time scale (t_d) for turbulence and the time (t_i) at which decaying magnetic turbulence becomes dominant are related as $t_i/t_d \simeq 14.8(B_0/\mathrm{nG})^{-1}(k_D/\mathrm{Mpc}^{-1})^{-1}$ (Chluba et al., 2015).

It is often assumed that, like the CMBR energy density, the primordial magnetic field and energy density scale with redshift z as $B(z) = B_0(1+z)^2$ and $\rho_B(z) \sim (1+z)^4$ respectively under magnetic flux freezing condition. However, the magnetic field energy continuously gets transferred to the IGM through the ambipolar diffusion and decaying turbulence processes. Therefore, we self-consistently calculate the redshift evolution of the magnetic field energy using the following equation,

$$\frac{d}{dz}\left(\frac{|\boldsymbol{B}|^2}{8\pi}\right) = \frac{4}{1+z}\left(\frac{|\boldsymbol{B}|^2}{8\pi}\right) + \frac{1}{H(z)\,(1+z)}(\Gamma_{\rm DT}+\Gamma_{\rm AD}). \tag{8}$$

The first term in the rhs quantifies the effect due to the adiabatic expansion of universe, and the second term quantifies the loss of the magnetic energy due to the IGM heating described above.

We simultaneously solve the above-mentioned equations to evaluate T_g and x_e for a range of possible values of the dark matter particle mass m_χ, the interaction cross-section $\sigma_{45} = \frac{\sigma_0}{10^{-45}\,\mathrm{m}^2}$, and the initial magnetic field (B_0) for a given $V_{\chi b}$. This analysis also provides the constraint on the magnitude of the magnetic field.

3.1 Results

Below we discuss our results on the heating due the primordial magnetic field in presence of the DM-b interaction. We set the following initial conditions at redshift $z_i = 1010$: $T_{\rm gi} = 2.725(1+z_i)\,\mathrm{K}$; $T_{\chi,i} = 0$, $V_{\chi b,i} = V_{\rm rms,i} = 29\,\mathrm{km/s}$, $B_i = B_0(1+z_i)^2$ and $x_{ei} = 0.055$ (obtained from RECFAST code[†] Seager et al., 1999, 2000).

Fig. 1 shows the evolution of the IGM temperature when both the primordial magnetic field and DM-baryon interactions are considered. The upper panel of Fig. 1 shows that the primordial magnetic field and DM-baryonic interaction together introduces a 'plateau like feature' in the

[†]http://www.astro.ubc.ca/people/scott/recfast.html

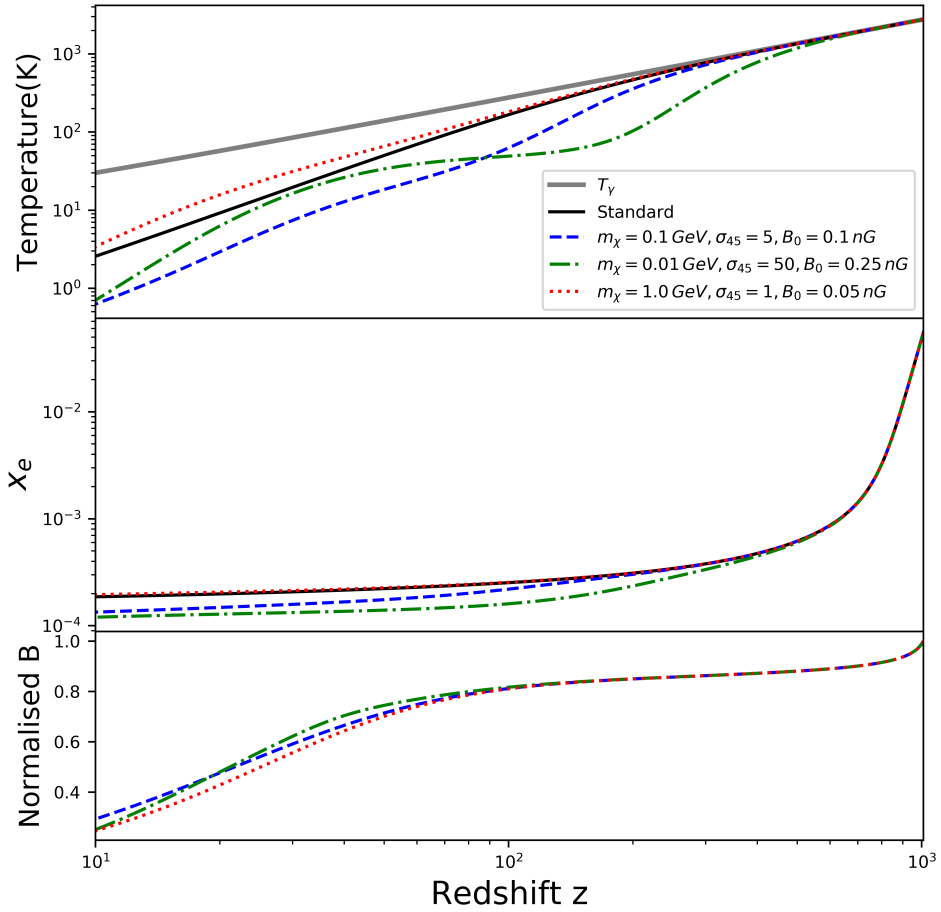

Figure 1: The upper and middle panels show the IGM kinetic temperature T_g and residual free electron fraction x_e as a function of redshift in presence of the primordial magnetic field and DM-baryon interaction. The solid black lines correspond to the primordial magnetic field with $B_0 = 0\,\mathrm{nG}$. The grey line in the upper panel shows the CMBR temperature T_γ. The lower panel shows the normalised magnetic field i.e. $\frac{B(z)}{B_0(1+z)^2}$ for the same B_0 values mentioned above.

redshift evolution of the IGM temperature for a certain range of model parameters m_χ, σ_{45} and B_0. One such example can be seen for $m_\chi = 0.01\,\mathrm{GeV}$, $\sigma_{45} = 50$ and $B_0 = 0.25\,\mathrm{nG}$ where the plateau like feature is seen in redshift range $\sim 50-150$. The cooling rate due to the DM-baryonic interaction and heating rate due to the primordial magnetic field compensates each other for a certain redshift range which gives the plateau like feature. At lower redshifts the heating due to the primordial magnetic field, which scales as $B^4(z)$, becomes ineffective as the primordial magnetic field decays very fast. This is both due to the adiabatic expansion of universe and loss of the magnetic energy due to heating. We notice that this plateau like feature is not so prominent for lower primordial magnetic field. This is a unique signature of the DM-baryonic

interaction in presence of the primordial magnetic field. However, it can only be probed by space-based experiment as it appears at the redshift range $\sim 50-150$.

The middle and lower panels of Fig. 1 show the residual electron fraction, x_e and primordial magnetic field, $B(z)$ as a function of redshift respectively. Like in previous cases, the residual electron fraction x_e is suppressed when both the DM-baryonic interactions and PMF are active. The suppressed residual electron fraction enhances the heating rate occurring due to the ambipolar diffusion. The primordial magnetic field looses its energy (other than the adiabatic loss because of universe's expansion) due to transfer of energy to IGM heating through the ambipolar diffusion process. This loss starts becoming important at lower redshifts $z \lesssim 100$.

We find that the primordial magnetic field with $B_0 \gtrsim 0.1\,\mathrm{nG}$ is ruled out in the standard scenario, but it can be well included within the allowed range when the interaction between DM and baryon with an appropriate parameter sets comes into play. In general, we find that the exact upper limit on the primordial magnetic field depends on the mass of the DM particles m_χ and the DM-baryonic interaction cross-section σ_{45}. We see that the primordial magnetic field with $B_0 \sim 0.4\,\mathrm{nG}$ is allowed for an appropriate set of m_χ and σ_{45}. As the primordial magnetic field decays very fast, the magnetic heating becomes ineffective at lower redshifts. The EDGES absorption spectra show that the IGM temperature is rising at redshifts $z \lesssim 17$. However, we find that the primordial magnetic field is not able to considerably heat up the IGM at the later phase of the cosmic dawn and, therefore, can not explain the heating part of the EDGES absorption profile. Hence, in the following section, we consider another possible source of heating, namely cosmic rays and describe its impact on the global HI 21-cm signal.

4 Impact of Cosmic ray protons during cosmic dawn and epoch of reionization[‡]

Cosmic rays are generated in the termination shock of the supernova explosions originated from both Pop III and Pop II stars. A significant fraction, $\epsilon \sim 0.15$ of the SNe kinetic energy ($E_{\rm SN}$) gets injected into the cosmic rays (Hillas, 2005; Caprioli & Spitkovsky, 2014). Thus the average rate of energy injection per unit physical volume into the cosmic rays (in units of erg $\mathrm{s}^{-1}\mathrm{cm}^{-3}$)

[‡]This section is adapted from the paper, "Impact of cosmic rays on the global 21-cm signal during cosmic dawn" by Bera et al. (2023b).

can be calculated as (Samui et al., 2005),

$$\dot{E}_{\rm CR}(z) = 10^{-30}\epsilon\left(\frac{E_{\rm SN}}{10^{51}\,{\rm erg}}\right) f_{\rm SN}\left(\frac{{\rm SFRD}(z)}{{\rm M_\odot\,yr^{-1}\,Mpc^{-3}}}\right)(1+z)^3. \tag{9}$$

Here the SFRD(z) is obtained from Eq. 10 for Pop III and Pop II stars using,

$${\rm SFRD}(z) = \int_z^\infty dz_c \int_{M_{\rm min}}^\infty dM' \dot{M}_*(M', z, z_c)\frac{d^2n(M', z_c)}{dz_c dM'}, \tag{10}$$

where z_c is the collapse redshift of the dark matter halos which is forming stars at a rate $\dot{M}_*$ at redshift $z < z_c$. Here, we assume that the redshift derivative of the differential halo mass function, $\frac{dn(M,z)}{dM}$ in equation 10 provides the formation rate of dark matter halos (Samui et al., 2009). Further, $M_{\rm min}$ is the lower mass cut-off of halos that can form stars. Note that, $\dot{M}_*$ depends on the halo mass M and the cooling mechanisms. Further, $f_{\rm SN}$ is the number of SNe explosion per unit solar mass of star formation.

In general, the cosmic ray proton spectra can be modelled as a power law in the momentum space (Schlickeiser, 2002) which is given by,

$$\frac{dn_{\rm CR}(p,z)}{dt}dp = \dot{N}_0(z)\left(\frac{p}{p_0}\right)^{-q}dp, \tag{11}$$

where, $\dot{N}_0(z)$ (along with p_0) is the normalisation factor which is determined from the total available energies of cosmic rays. It is calculated by integrating $E(p)\dot{N}_0(p/p_0)^{-q}dp$ with a low energy cut-off of 10 keV and equating to $\dot{E}_{\rm CR}(z)$ (Eq. 9). The slope of the spectrum, q has a typical value of 2.2 (Schlickeiser, 2002) which matches quite well with observations. The physical number density of cosmic rays at a redshift z, having velocity between β and $\beta + d\beta$ is given by,

$$N_{\rm CR}(\beta, z, z_0) = \int_{z_0}^{z} dz_i \frac{dn(z_i, p_i)}{dz_i}\frac{dp_i}{d\beta_i}\frac{d\beta_i}{d\beta}\left(\frac{1+z}{1+z_i}\right)^3. \tag{12}$$

Here, z_0 is the initial redshift of cosmic ray injection by the first generation of stars and we have taken it to be $z = 50$. Cosmic ray protons are expected to loose their energy while propagating from redshift z_i to z. The redshift evolution of velocity $v = \beta c$ of cosmic ray particles is governed by three processes, (i) the collision with free e^-, (ii) ionization of neutral hydrogen, and (iii) the adiabatic expansion of the universe, and is given by (Schlickeiser, 2002),

$$\begin{aligned}\frac{d\beta}{dz} = \frac{1}{H(z)\,(1+z)}\Bigg[&3.27\times10^{-16}n_e(z)\frac{(1-\beta^2)^{3/2}}{\beta}\frac{\beta^2}{x_m^3+\beta^3}\\ &+1.94\times10^{-16}n_{\rm HI}(z)\frac{(1-\beta^2)^{3/2}}{\beta}\frac{2\beta^2}{(0.01)^3+2\beta^3}\\ &\times\{1+0.0185\log\beta\,\Theta(\beta-0.01)\}\Bigg]+\frac{\beta(1-\beta^2)}{(1+z)}\end{aligned} \tag{13}$$

where, $n_e(z)$ and $n_{\rm HI}(z)$ are the electron and neutral hydrogen densities respectively in units of cm^{-3}, $x_m = 0.0286(T_g/(2\times10^6\,{\rm K}))^{1/2}$ and Θ is the Heaviside step function.

Further, the heating rate of the IGM by cosmic ray particles due to ionization can be written as,

$$\Gamma_{\rm CR}(z, z_0) = \frac{5}{8}\eta_1\eta_2\eta_3 \int \frac{dE(\beta)}{dz} N_{\rm CR}(\beta, z, z_0)\, d\beta, \tag{14}$$

where, $\eta_1 = 5/3$ occurs due to the secondary ionization by e^- which produces during ionization by primary cosmic ray particles, $\eta_2 \simeq 1.17$ accounts the 10% He abundance in the IGM, and $\eta_3 \simeq 1.43$ takes into account the contribution of heavy cosmic ray nuclei and cosmic ray electrons (e^-), positrons (e^+) (Schlickeiser, 2002). The energy depositions due to the cosmic ray particles are taken into account in the temperature evolution of IGM i.e. in Eq. 4 and we find that they can contribute as a major heating source of IGM during the cosmic dawn that is described in the following section.

4.1 Results

We assume a single star of 145 $M_\odot$ is formed in minihalos and explodes as a supernova having energy 10^{52} erg (mid mass range of Mebane et al., 2018). Thus in our model, $f^{\rm SN} \approx 1/145$ and $E_{\rm SN} \sim 10^{52}$ erg for Pop III stars. In case of Pop II stars, we assume that a supernova of energy $E_{\rm SN} \sim 10^{51}$ erg is formed per 50 $M_\odot$ of a star having $1-100$ $M_\odot$ of Salpeter IMF and hence, $f_{\rm SN} = 0.02$ (Samui et al., 2005).

In Fig. 2, we show the changes in gas temperature, spin temperature, and resulting 21-cm brightness temperature at the top, middle and bottom panels respectively by varying our model parameters such as q, $\epsilon_{\rm III}$, and $\epsilon_{\rm II}$ that govern the energy deposition by cosmic ray particles into the IGM from both Pop III and Pop II stars. The left panels of Fig. 2 show results in presence of the dark matter-baryon interaction with dark matter mass $m_\chi = 0.1$ GeV and the interaction cross-section $\sigma_{45} = 2$. The right panel shows results in the standard scenario without the dark matter-baryon interaction. In the top and middle panels, the black dotted curves represent the CMBR temperature. The black dashed curve in the top panel is the gas temperature where no cosmic ray heating is considered and the corresponding spin temperature is shown in the middle panel by black dashed curve for reference. The variation w.r.t the cosmic ray spectral index q is shown by magenta lines where we consider a shallower slope of $q = 2.1$. Given the same energy input, the number of cosmic ray particles below 30 MeV decreases for a smaller q. These are the particles that take part in the collisional heating and hence the flatter slope makes

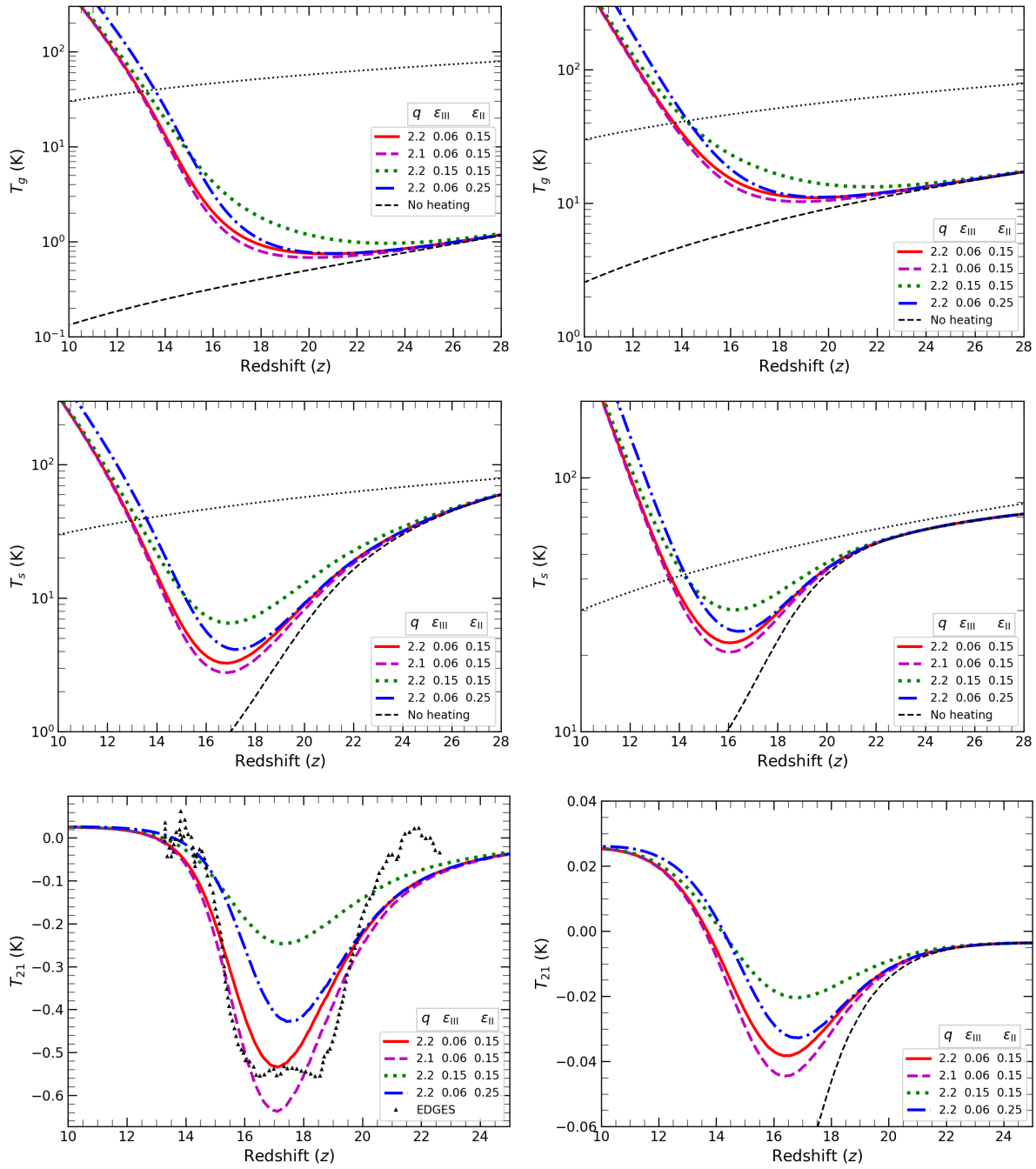

Figure 2: **Left panel:** The impact of cosmic ray heating on T_g, T_s and resulting T_{21} (upper to lower) are shown for different parameters describing the efficiencies of cosmic ray heating. The inset values represent the spectral index of cosmic ray spectra, q, the efficiencies of heating due to cosmic rays generated from Pop III and Pop II stars, $\epsilon_{\rm III}$ and $\epsilon_{\rm II}$ respectively. We keep the other parameter, $Q_{{\rm CR},II} = \epsilon_{\rm II}$ for this figure. In this panel the evolution of temperatures are done in the extra cooling scenario due to dark matter-baryon interaction in light of EDGES observation. The black dotted curves in the upper and middle panel represent the CMBR temperature, T_γ, whereas the black dashed curves are the temperatures where no heating source is present. **Right panel:** Same as left panel but in absence of any dark matter-baryon interaction.

the cosmic ray heating less efficient as can be seen from the figure. This further increases the absorption depth in 21-cm signal as can be seen from bottom panel.

In the right panels of Fig. 2, we show our results without considering any dark matter-baryon interaction. All other parameters are the same as in the left panels of the figure. As expected, in general the IGM temperature is much higher having a minimum value of ~ 10 K by $z \sim 17$ for our default parameter set (solid red curves). This resulted in a spin temperature of ~ 20 K due to the Ly-α coupling. Afterwards, the IGM temperature and hence T_s increases due to the rapid cosmic ray heating. Finally T_s crosses the CMBR temperature by $z \sim 14$ which leads to a weaker absorption profile of maximum ~ -0.04 K as can be seen from bottom right panel. The exact position of the absorption maxima depends on the interplay of Ly-α coupling and the onset of cosmic ray heating.

We find that the cosmic rays can dissipate their energy to the IGM within Hubble time to influence the IGM temperature of 10 K at $z \sim 15$. We note that the Pop II stars are likely to heat the IGM by magnetosonic heating which is sensitive to the IGM magnetic field. Hence, this magnetosonic transfer of energy due to cosmic rays is an important source of IGM heating. The exotic dark matter-baryon interaction is considered to explain the unusually strong absorption profile detected by EDGES group. However, cosmic ray heating is a more generic physics that one should consider while modeling the cosmic 21-cm signal. It is likely to play an important role in shaping the global HI 21-cm signal. In particular, it is likely to reduce the depth of any absorption signal if at all present. However, as already mentioned, the cosmic ray heating is directly proportional to the efficiency parameters, any future observation of 21-cm signal from redshift $z \sim 14-20$ can be used to tightly constrain early star formation, and the corresponding cosmic ray heating efficiencies.

Currently, there is only one observation of global HI 21-cm signal by Bowman et al. (2018) along with a null detection by Singh et al. (2021) during cosmic dawn. However, there are several observational constraints exist during the reionization and post-reionization epochs. Hence, in the following section, we combine most of the available observations from cosmic dawn and the epoch of reionization to explore the prospects of bridging the gap between these two epochs.

5 Bridging the gap between cosmic dawn and epoch of reionization[§]

The observational global constraints on reionization at $z \gtrsim 5$, include measurements of the volume-averaged neutral hydrogen fraction of the IGM ($x_{\rm HI}$) using different techniques such as the evolution in Lyman-α and Lyman-β forests (Fan et al., 2001; White et al., 2003; McGreer et al., 2015) and Lyman-α emitters (Ouchi et al., 2010; Zheng et al., 2011; Mesinger et al., 2014; Sobacchi & Mesinger, 2015; Mason et al., 2019), the optical depth (τ) to Thomson scattering of cosmic microwave background (CMB) photons as measured by Planck Collaboration et al. (2020b), and the ionizing emissivity ($\dot{N}_{\rm ion}$) constraints as compiled by Becker & Bolton (2013). However, more stringent constraints are expected from the 21-cm measurements, which will play a crucial role to map out the HI distribution to trace the large-scale structure.

On the other hand, the constraints on cosmic dawn come from the measurements of the 21-cm global signal at $z > 15$. At this epoch, the controversial EDGES detection (Bowman et al., 2018) of a flattened absorption profile in the sky-averaged radio spectrum, centered at 78 MHz with an amplitude of 0.5 K, provides a tentative constraint on the 21-cm global signal during cosmic dawn. Inferred from the EDGES signal, Madau (2018) have derived a constraint on the early star formation and shown that it is consistent with an extrapolation of UV measurements at lower redshifts ($4 < z < 9$). While there have been many theoretical (see e.g., Hills et al., 2018; Bradley et al., 2019; Singh & Subrahmanyan, 2019; Sims & Pober, 2020) and observational works (see e.g., Singh et al., 2022) suggesting that the measured profile by EDGES may not be of astrophysical origin, it remains crucial to understand what implications such a detection might have on cosmic dawn and reionization. In particular, could additional constraints be placed on the role of faint and bright galaxies during these epochs if the measurement holds? In light of the recent successful launch of the James Webb Space Telescope (JWST) and the growing observational efforts to detect the 21-cm signal during cosmic dawn, many high-redshift constraints are expected, and hence it is currently a scientific priority to ask the question: What is required to bridge the gap between cosmic dawn and reionization?

We here use a semi-analytical approach coupled with a Markov Chain Monte Carlo (MCMC) sampler to explore the range of scenarios and models that are mostly consistent with the

[§]This section is adapted from the paper, "Bridging the Gap between Cosmic Dawn and Reionization favors Faint Galaxies-dominated Models" by Bera et al. (2022).

combined constraints from cosmic dawn and reionization. Since all considered constraints are globally-averaged quantities, a semi-analytical approach is sufficiently accurate. In this model, the ionization rate $R_{\rm ion}$ is parameterized as a function of halo mass (M_h) and redshift (z). The mass dependence of $R_{\rm ion}$ is analogous to the Schechter function, which can be characterized as a power law on the bright end and an exponential cut-off on the faint end. The redshift dependence follows a simple power law. This parameterization of $R_{\rm ion}$ accounts for the non-linear dependence on halo mass, which can be expressed as follows:

$$\frac{R_{\rm ion}}{M_h} = A\,(1+z)^D \left(\frac{M_h}{B}\right)^C \exp\left[-\left(\frac{M_h}{B}\right)^{-3}\right], \tag{15}$$

where A, B, C, and D are free parameters, and their best-fit values were obtained by calibrating to radiative transfer simulations. We refer the reader to Hassan et al. (2016) for more details about the derivation of this model. Having defined our source model $R_{\rm ion}$, we adopt the Sheth & Tormen (1999) halo mass function ($\frac{{\rm d}n}{{\rm d}M}$), which provides the number density of halos per unit halo mass, to compute the cosmic evolution of the global quantities governing reionization and comic dawn.

5.1 Results

In this work, we consider the halo mass range from 10^5 to $10^{15}\,{\rm M}_\odot$ to account for the contribution from all source populations including the most faint halos. The most interesting parameters of this source model are the B and C parameters, since they allow us to draw conclusions about the role of different source populations during cosmic dawn and reionization. Therefore, we set the amplitude $A = 10^{40}\,{\rm M}_\odot^{-1}{\rm s}^{-1}$ and redshift index $D = 2.28$, following the calibration to radiative transfer simulations throughout.

The reionization constraints include the $\dot{N}_{\rm ion}$, $x_{\rm HI}$, and τ data. As mentioned earlier, the only existing constraint during cosmic dawn comes from the EDGES detection at $z \sim 17$, from which Madau (2018) have been able to place constraints on the UV luminosity density $\rho_{\rm UV}$. We constrain our source model to reionization only constraints ($\dot{N}_{\rm ion} + x_{\rm HI} + \tau$), and combined reionization and cosmic dawn constraints ($\dot{N}_{\rm ion} + x_{\rm HI} + \tau + \rho_{\rm UV}$). We refer to the former as EoR($\dot{N}_{\rm ion} + x_{\rm HI} + \tau$), and to the later as CD(EDGES) + EoR($\dot{N}_{\rm ion} + x_{\rm HI} + \tau$). We compare the two resulting posterior distributions in Figure 3. Blue and red correspond to reionization only (EoR) and cosmic dawn plus reionization (CD+EoR), respectively. In both cases, combined observations place tight constraints on our parameters but in different parts of the parameter

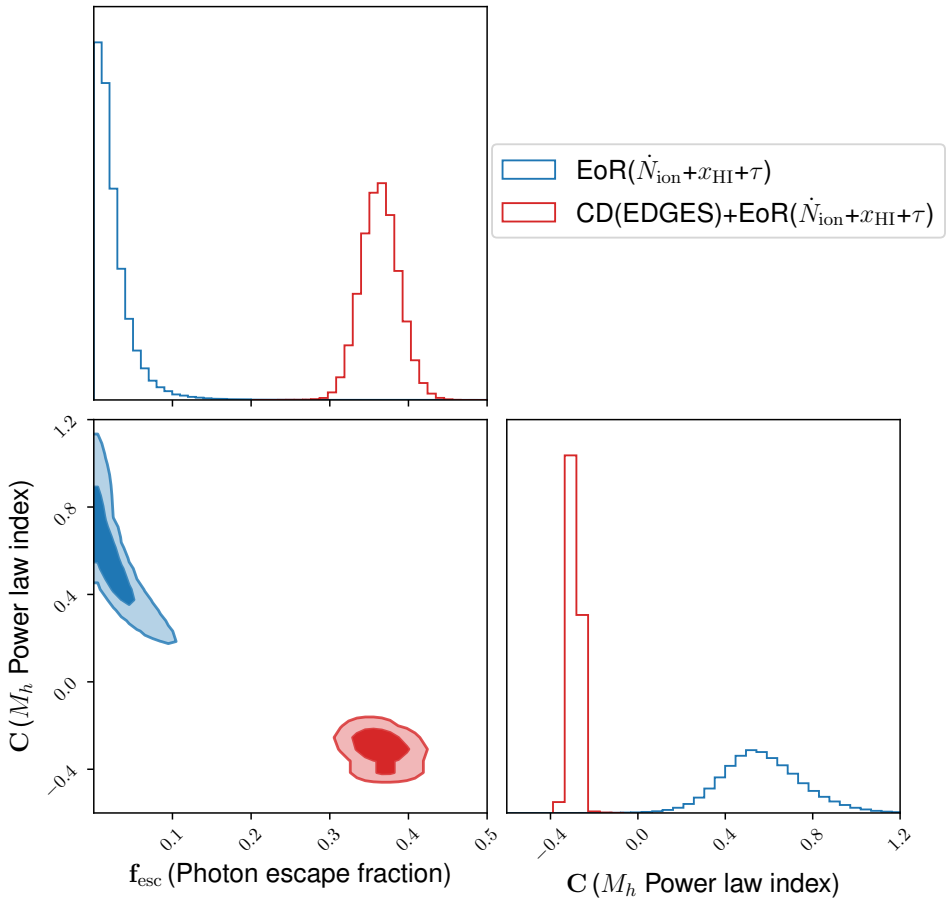
EoR($\dot{N}_{\rm ion}$+$x_{\rm HI}$+τ)
CD(EDGES)+EoR($\dot{N}_{\rm ion}$+$x_{\rm HI}$+τ)
C (M_h Power law index)
$f_{\rm esc}$ (Photon escape fraction)
C (M_h Power law index)

Figure 3: Comparison between the combined constraints from reioniztion, EoR ($\dot{N}_{\rm ion}, x_{\rm HI}, \tau$) in blue, and by adding cosmic dawn to reionization, CD ($\rho_{\rm UV}$ from EDGES) + EoR ($\dot{N}_{\rm ion}, x_{\rm HI}, \tau$) in red. The dark and light shaded contours correspond to the 1σ and 2σ levels, respectively.

space. We find that the reionization combined observations (blue, EoR) are mainly driven by the reionization history measurements ($x_{\rm HI}$). This shows that constraining to reionization observations favors models with low $f_{\rm esc}$ and positive C, indicating that massive galaxies play a major role to drive reionization. On the other hand, constraining to both reionization and cosmic dawn observations (red, CD+EoR) favors models with high $f_{\rm esc}$ and negative C, suggesting that low-mass galaxies play a dominant role to bridge the gap between these two epochs. This is represented by the diagonal shift from the blue to red contours once the cosmic dawn constraint is added to the likelihood.

We then compare our predictions with results from the THESAN project (Kannan et al., 2022; Garaldi et al., 2022; Smith et al., 2022), which provides a suite of radiation-magneto-hydrodynamic simulations that self-consistently evolve reionization on large-scales ($L_{\rm box}$ = 95.5 cMpc) and resolve the majority of ionizing sources responsible for it ($m_{\rm gas} = 5.82 \times 10^5 {\rm M}_\odot$)

with galaxy formation physics based on the state-of-the-art IllustrisTNG model. Specifically, we compare with the THESAN-HIGH and THESAN-LOW simulation runs, where reionization is mainly driven by high-mass and low-mass galaxies, respectively and we find that our models (EoR, CD+EoR) and the different THESAN runs are consistent within the 1–2σ levels.

6 Summary and Conclusions

This thesis work is dedicated to study the impacts of several physical processes on cosmological HI 21-cm signal, in particular, on the global HI 21-cm signal. Starting with the modelling of the first generation of stars/galaxies, the evolution and energy deposition by magnetic fields and cosmic rays into the IGM have been studied with emphasis on the observational constraints obtained by EDGES. Moreover, the reionization constraints are combined with the cosmic dawn constraints to highlight the parameter space constrained by the joint observations that can further be verified by ongoing and upcoming surveys like JWST and SKA respectively.

Studying the role of the primordial magnetic field on the background of colder IGM in sec. 3, at first we find that the magnetic field suppresses the abundance of the residual free electron fraction x_e which, in turn, enhances the rate of IGM heating through the ambipolar diffusion. Second, the coupling coefficient between the ionised and neutral components $\gamma(T_g)$ decreases with the IGM temperature, which again results in the increased heating rate (see eq. 6). Moreover, the heating rate due to the Compton process, which is proportional to $(T_\gamma - T_g)$ and x_e, too gets affected when the background IGM temperature T_g is lower (eq. 4). We find that collectively all these effects make the heating rate due the magnetic field faster in the colder background in compare to the heating rate in the standard scenario. Consequently, the primordial magnetic field decays, with redshift, at much faster rate compared to the simple $(1+z)^2$ scaling during the dark ages and cosmic dawn. The decay is particularly significant for $B_0 \lesssim 0.5\,\mathrm{nG}$ when the fractional change in the magnetic field due to the heating loss could be $\sim 50\%$ or higher and this is unique in the colder IGM scenario. Furthermore, we find that the upper limit on the primordial magnetic field using the EDGES measurements is determined by the underlying non-standard cooling process, i.e., the DM-baryon interaction here. For example, the primordial magnetic filed with $B_0 \sim 0.4\,\mathrm{nG}$ which is ruled out in the standard model (Minoda et al., 2019), may be allowed if the DM-baryon interaction with $m_\chi = 0.01\,\mathrm{GeV}$ and $\sigma_{45} = 100$ is included. However, we find that the primordial magnetic field with $B_0 \gtrsim 1\,\mathrm{nG}$

may not be allowed as this requires very efficient cooling of the IGM which is unlikely to occur even for very strong possible DM-baryon interaction.

In sec. 4, we present the heating by cosmic rays generated from the early generation of stars. In our model, we take into account both metal free Pop III and metal enriched Pop II stars. We also consider the meta-galactic Lyman-Werner feedback on the Pop III stars along with supernova feedback in Pop II galaxies in order to calculate the star formations. The temperature evolution of IGM has been calculated using the cosmic ray heating along with the dark matter-baryon interaction and adiabatic cooling. We consider the ionization and collisional heating by low energy cosmic ray protons generating and escaping from Pop III halos. This is contrary to massive atomic cooling halos hosting Pop II stars where the low energy protons get confined within the halo and only high energy protons can escape into the IGM and contribute to the heating. We note that the major part of the cosmic ray energy is carried by the high energy protons (~ 1 GeV). We find that the cosmic ray is an important source of IGM heating and shapes the global HI 21-cm signal during cosmic dawn which is in agreement with the existing literature. The depth, duration and timing of the absorption signal are highly modulated by the cosmic ray heating that we consider here. In particular, the EDGES signal can be well explained by our model of cosmic ray heating along with the Ly-α coupling and dark matter-baryon interaction with a suitable choice of efficiency parameters.

Using a semi-analytical framework of reionization with a physically-motivated source model coupled with MCMC likelihood sampling in sec. 5, our key findings are as follows: i. Calibrating our source model $R_{\rm ion}$ to cosmic dawn constraints ($\rho_{\rm UV}$ from EDGES) favors models with the stronger contribution from low-mass (faint) galaxies. This is required to reproduce the inferred $\rho_{\rm UV}$ constraints from EDGES. ii. Constraining our source model $R_{\rm ion}$ to different reionization observables is mainly driven by the IGM neutral fraction measurements where models with low escape fraction and dominated by massive galaxies are favored. This suggests that the bright galaxies play the major role to drive reionization. iii. Further constraining our source model $R_{\rm ion}$ to both reionization ($\dot{N}_{\rm ion} + x_{\rm HI} + \tau$) and the cosmic dawn constraint ($\rho_{\rm UV}$ from EDGES) favors models with high escape fraction and dominated by low-mass galaxies. This implies that faint galaxies would play a crucial role to bridge the gap between cosmic dawn and reionization. iv. Massive (bright) galaxies-dominated models produce an increasing emissivity that results in a later onset of reionization, more sudden and shorter reionization duration, and lower optical depth. Low-mass (faint) galaxies-dominated models result in a flatter emissivity evolution with

the opposite reionization history characteristics. As demonstrated by the CD+EoR model, it is entirely possible to reconcile the different observational constraints from the cosmic dawn to post-reionization using faint galaxies-dominated models of reionization, without the need to invoke new physics/exotic sources to explain the potential detection by EDGES. Our results shed additional light on the roles of faint and bright galaxies during cosmic dawn and reionization, which can be tested by upcoming JWST surveys.

7 Future outlook

In this thesis work, we discussed two heating mechanisms that impact the global HI 21-cm signal during different epochs. However, as mentioned earlier there are other processes that are likely to affect the heating of the inter-galactic medium such as X-rays, Ly-α, CMB, etc. At present, there is no evidence showing the domination of any heating mechanism over others. All possible heating mechanisms have their own free parameters which are not well-constrained. Hence, we aim to do a comprehensive study of the different heating processes of IGM in the future. This is required to understand if the impact of different heating processes and their sources could be differentiated from the time evaluation of 21-cm signal. If we find that the global signal is not adequate to provide this information, we will further look into the 21-cm power spectrum fluctuations. In future surveys, when more observational evidences are available, detailed modeling of 21-cm signal including all possible sources of heating is effective.

References

Abdurashidova Z., et al., 2022, Ap.J, 924, 51

Ali S. S., Bharadwaj S., Chengalur J. N., 2008, MNRAS, 385, 2166

Barkana R., 2018, Nature, 555, 71

Barkana R., Loeb A., 2005, The Astrophysical Journal, 626, 1

Beardsley A. P., et al., 2016, Ap.J, 833, 102

Becker G. D., Bolton J. S., 2013, MNRAS, 436, 1023

Bera A., Datta K. K., Samui S., 2020, MNRAS, 498, 918

Bera A., Hassan S., Smith A., Cen R., Garaldi E., Kannan R., Vogelsberger M., 2022, arXiv e-prints, p. arXiv:2209.14312

Bera A., Ghara R., Chatterjee A., Datta K. K., Samui S., 2023a, Journal of Astrophysics and Astronomy, 44, 10

Bera A., Samui S., Datta K. K., 2023b, MNRAS, 519, 4869

Bowman J. D., Rogers A. E. E., Monsalve R. A., Mozdzen T. J., Mahesh N., 2018, Nature, 555, 67

Bradley R. F., Tauscher K., Rapetti D., Burns J. O., 2019, Ap.J, 874, 153

Caprioli D., Spitkovsky A., 2014, Ap.J, 783, 91

Chluba J., Paoletti D., Finelli F., Rubiño-Martín J. A., 2015, MNRAS, 451, 2244

Chuzhoy L., Shapiro P. R., 2006, Ap.J, 651, 1

Cooray A., et al., 2019, BAAS, 51, 48

Das A., Mesinger A., Pallottini A., Ferrara A., Wise J. H., 2017, MNRAS, 469, 1166

Datta K. K., Kundu A., Paul A., Bera A., 2020, arXiv e-prints, p. arXiv:2001.06497

De E., Acedo E., 2019, REACH: Radio Experiment for the Analysis of Cosmic Hydrogen

DeBoer D. R., et al., 2017, PASP, 129, 045001

Ewall-Wice A., Chang T.-C., Lazio T. J. W., 2020, MNRAS, 492, 6086

Fan X., et al., 2001, ASTRON J, 122, 2833

Fialkov A., Barkana R., Visbal E., 2014, Nature, 506, 197

Field G. B., 1958, Proceedings of the IRE, 46, 240

Field G. B., 1959, Ap.J, 129, 551

Furlanetto S. R., Oh S. P., Briggs F. H., 2006a, Physics Reports, 433, 181

Furlanetto S. R., Oh S. P., Briggs F. H., 2006b, PHYS REP, 433, 181

Garaldi E., Kannan R., Smith A., Springel V., Pakmor R., Vogelsberger M., Hernquist L., 2022, MNRAS, 512, 4909

Ghara R., Mellema G., 2020, MNRAS, 492, 634

Ginzburg V. L., Ozernoi L. M., 1966, Sovast, 9, 726

Hassan S., Davé R., Finlator K., Santos M. G., 2016, MNRAS, 457, 1550

Hillas A. M., 2005, Journal of Physics G Nuclear Physics, 31, R95

Hills R., Kulkarni G., Meerburg P. D., Puchwein E., 2018, Nature, 564, E32

Hirata C. M., 2006, MNRAS, 367, 259

Kannan R., Garaldi E., Smith A., Pakmor R., Springel V., Vogelsberger M., Hernquist L., 2022, MNRAS, 511, 4005

Kompaneets A. S., 1957, Soviet Journal of Experimental and Theoretical Physics, 4, 730

Kunze K. E., Komatsu E., 2014, JCAP, 2014, 009

Ma Q.-B., Ciardi B., Eide M. B., Busch P., Mao Y., Zhi Q.-J., 2021, Ap.J, 912, 143

Madau P., 2018, MNRAS, 480, L43

Madau P., Meiksin A., Rees M. J., 1997, Ap.J, 475, 429

Mason C. A., et al., 2019, MNRAS, 485, 3947

McGreer I. D., Mesinger A., D'Odorico V., 2015, MNRAS, 447, 499

Mebane R. H., Mirocha J., Furlanetto S. R., 2018, MNRAS, 479, 4544

Mebane R. H., Mirocha J., Furlanetto S. R., 2020, MNRAS, 493, 1217

Mellema G., Koopmans L., Shukla H., Datta K. K., Mesinger A., Majumdar S., 2015, Advancing Astrophysics with the Square Kilometre Array (AASKA14), p. 10

Mertens F. G., et al., 2020, MNRAS, 493, 1662

Mesinger A., Aykutalp A., Vanzella E., Pentericci L., Ferrara A., Dijkstra M., 2014, Monthly Notices of the Royal Astronomical Society, 446, 566

Minoda T., Hasegawa K., Tashiro H., Ichiki K., Sugiyama N., 2017, PHYS REV D, 96, 123525

Minoda T., Tashiro H., Takahashi T., 2019, Monthly Notices of the Royal Astronomical Society, 488, 2001

Mittal S., Kulkarni G., 2021, MNRAS, 503, 4264

Muñoz J. B., Loeb A., 2018, Nature, 557, 684

Muñoz J. B., Kovetz E. D., Ali-Haïmoud Y., 2015, PHYS REV D, 92, 083528

Ouchi M., et al., 2010, The Astrophysical Journal, 723, 869

Padmanabhan H., 2021, International Journal of Modern Physics D, 30, 2130009

Pal S., Bharadwaj S., Ghosh A., Choudhuri S., 2021, MNRAS, 501, 3378

Patil A. H., et al., 2017, Ap.J, 838, 65

Patwa A. K., Sethi S., Dwarakanath K. S., 2021, MNRAS, 504, 2062

Peebles P. J. E., 1968, Ap.J, 153, 1

Peebles P. J. E., 1993, Principles of Physical Cosmology

Planck Collaboration et al., 2020a, A & A, 641, A6

Planck Collaboration et al., 2020b, A & A, 641, A6

Price D. C., et al., 2018, MNRAS, 478, 4193

Pritchard J. R., Furlanetto S. R., 2006, MNRAS, 367, 1057

Pritchard J. R., Furlanetto S. R., 2007, MNRAS, 376, 1680

Pritchard J. R., Loeb A., 2012, Reports on Progress in Physics, 75, 086901

Samui S., Subramanian K., Srianand R., 2005, in 29th International Cosmic Ray Conference (ICRC29), Volume 9. p. 215 (arXiv:astro-ph/0505590)

Samui S., Subramanian K., Srianand R., 2009, NEW ASTRON, 14, 591

Sazonov S., Sunyaev R., 2015, MNRAS, 454, 3464

Schlickeiser R., 2002, Cosmic Ray Astrophysics

Seager S., Sasselov D. D., Scott D., 1999, Ap.JL, 523, L1

Seager S., Sasselov D. D., Scott D., 2000, Ap.JS, 128, 407

Sethi S. K., Subramanian K., 2005, MNRAS, 356, 778

Sheth R. K., Tormen G., 1999, MNRAS, 308, 119

Sims P. H., Pober J. C., 2020, MNRAS, 492, 22

Singh S., Subrahmanyan R., 2019, Ap.J, 880, 26

Singh S., et al., 2021, arXiv e-prints, p. arXiv:2112.06778

Singh S., et al., 2022, Nature Astronomy, 6, 607

Smith A., Kannan R., Garaldi E., Vogelsberger M., Pakmor R., Springel V., Hernquist L., 2022, MNRAS, 512, 3243

Sobacchi E., Mesinger A., 2015, Monthly Notices of the Royal Astronomical Society, 453, 1843

Venumadhav T., Dai L., Kaurov A., Zaldarriaga M., 2018, PHYS REV D, 98, 103513

White R. L., Becker R. H., Fan X., Strauss M. A., 2003, The Astronomical Journal, 126, 1

Wouthuysen S. A., 1952, ASTRON J, 57, 31

Xu Y., Yue B., Chen X., 2021, Ap.J, 923, 98

Zheng Z., Cen R., Trac H., Miralda-Escudé J., 2011, Ap.J, 726, 38